IN FOCUS: NANOMEDICINE - ARTICLE

Understanding Nano-Anatomy of Healthy and Carious Human Teeth: a Prerequisite for Nanodentistry

Sebastian Gaiser · Hans Deyhle · Oliver Bunk ·
Shane N. White · Bert Müller

Abstract The anatomy of human teeth reflects its usage. Spatially resolved X-ray scattering permits quantitative studies of the characteristic arrangement of the anisotropic calcium phosphate crystallites and the collagen fibers within the hard tissues of the crown. The present study summarizes the distinctive nanometer-sized anatomical features of the tooth hard tissues including their interface taking advantage of spatially resolved synchrotron radiation-based small-angle X-ray scattering. The comparison of slices from eight teeth indicates a long-range organization of tooth nanostructures.

Abbreviations

3D	Three dimensional
AFM	Atomic force microscopy
bl	Buccal–lingual
DEJ	Dentin enamel junction
FDI	World dental federation
FFT	Fast Fourier transform
md	Mesial–distal
SAXS	Small-angle X-ray scattering
SEM	Scanning electron microscopy
SRμCT	Synchrotron radiation-based micro computed tomography

S. Gaiser · H. Deyhle · B. Müller (✉)
Biomaterials Science Center, University of Basel,
University Hospital, 4031 Basel, Switzerland
e-mail: bert.mueller@unibas.ch

H. Deyhle · O. Bunk
Swiss Light Source, Paul Scherrer Institut,
5232 Villigen PSI, Switzerland

S. N. White
UCLA School of Dentistry, University of California,
Los Angeles, CA 90095-3075, USA

1 Introduction

Quality of life implicates proper nutrition presuming long-term oral health, which is associated with the number of teeth in the dentition [1]. Elderly patients with more than 20 remaining teeth experience a superior subjective physical health score to those with less than 20 teeth [2]. In highly developed mammals, teeth are a limiting life factor, as they are necessary for nutrition. Teeth are subject to high wear and mechanical loads resulting from biting forces of approximately 500 N and biting pressures of up to 34 MPa [3] for decades. Unlike other hard tissues, e.g. bone, remodeling does not occur in human teeth with the exception of relatively minor secondary dentin formation [4]. Human tooth crowns consist of dentin as supporting core, which is composed of highly mineralized peri-tubular dentin surrounded by less mineralized inter-tubular dentin [5]. The well defined, oriented microtubules of dentin display anisotropy on the micrometer scale. Dentin abuts on dental enamel and acts as energy-absorbing, crack-resistant structure [6]. Much effort has been devoted to understand the detailed composition and the microstructure of tubules [7–12], as well as their relationship to fracture toughness [6, 13]. The interface between dentin and enamel, i.e. the dentin–enamel junction (DEJ) [14] is of particular interest. Here, the two hard tissues with very different biomechanical properties are robustly joined. Enamel is hard and brittle, whereas dentin is much tougher and less stiff. The DEJ exhibits remarkable mechanical properties transferring the loads from enamel to dentin [15]

and providing a crack-arrest barrier [16]. Pioch et al. [17], for example, measured the shear strength along the DEJ and were unable to detect any fracture along this interface. Cracks initiated in enamel went straight through the DEJ rather than along [18]. Cracks tended to penetrate the (optical) DEJ and arrested in the tough mantle dentin [13], where damage was spread over a broad zone [19]. Gap bridging at the crack tip was reported to be the main crack-arresting mechanism [13]. There is common agreement that the DEJ is not an interface in mathematical sense but rather an extended transition region. Different reports on the DEJ width show variation in intra-tooth location [20–23].

Enamel, the outmost part of human tooth crowns and the hardest tissue in the human body, is composed of 92–96 wt% inorganic and approximately 4 wt% of organic substance [24]. The inorganic phases mainly consist of calcium phosphates including carbonated hydroxyapatite and fluoridated hydroxyapatite [25]. The hydroxyapatite in enamel is arranged in crystallites bundled in rods, which run from the DEJ to the tooth surface. The space between rods, termed inter-rod enamel, contains more organic material than the rods themselves [26]. White et al. [27] showed the importance of biological organization, stating that fracture toughness of enamel is three times larger than that of pure apatite crystallites. They concluded that the composition of the crown and its microanatomy limit crack growth along the rods. Thus, the complex three-dimensional (3D) organization of the hard tissues from the nanometer to the macroscopic scales confers such outstanding mechanical properties upon tooth structure. The complex structure of human teeth [28–32] facilitates the preservation of hardness and wear resistance over many millions of masticatory cycles. Besides the microscopic structure, investigations of the nanostructure have been performed, mainly with local probe techniques including atomic force microscopy (AFM) and scanning electron microscopy (SEM) [22, 33–36]. Due to the reduced field of view, however, only restricted parts of the tooth of interest can be examined. In addition, these techniques only permit the investigation of surfaces. The bulk structures including the internal interfaces are not directly accessible. Therefore, the understanding of the tooth-wide organization down to the nanometer level, which relates to vital components such as hydroxyapatite crystallites and collagen fibers, remains vague. X-ray-based scattering techniques are well suited to reveal bulk nanostructures. Position-resolved small-angle X-ray scattering (often termed scanning SAXS) [37, 38] is a unique method for investigating nanostructures of healthy and carious teeth over macroscopic areas [31, 32, 39, 40].

It is hypothesized that scanning SAXS will yield, beside several known features, a description of the entire nanostructure of a tooth slice. Comparing a series of non-carious and carious teeth may reveal characteristic nanostructures

of healthy and diseased human teeth. This knowledge could provide a basis for treating carious teeth in a biomimetic manner for example using calcium phosphate particles of nanometer size to re-mineralize the hard tissues in hardly affected lesions.

2 Materials and Methods

2.1 Specimen Characterization

Eight human teeth, six with and two without visible carious lesions, from different patients, extracted for clinical reasons, were included in this study. Prior to cutting, necessary for two-dimensional (2D) scanning SAXS experiments, micro computed tomography data of the entire teeth were acquired with a SkyScan 1174™ (SkyScan, Kontich, Belgium) tabletop scanner, allowing to determine the exact location of the slices within the tooth. The pixel size ranged from 17.5 to 28.8 μm. 1,201 projections with equal angular steps over 360° were acquired with 3 s exposure time per projection. A 0.5 mm-thick Al filter was placed in the beam path to increase the mean photon energy and to reduce beam hardening. The data were reconstructed with the software NRecon (SkyScan, Kontich, Belgium) using a modified Feldkamp algorithm.

2.2 Specimen Preparation

Three to ten 200–500 μm thin slices parallel to the tooth axis were cut from each tooth with a diamond band saw (Exact Apparatebau GmbH, Norderstedt, Germany), an example is illustrated in Fig. 1. Prior to SAXS and SRμCT measurements, the specimens were stored in 0.9% NaCl solution and air, respectively. Table 1 gives an overview of the specimen locations in the dentition and the slice cut direction (md, mesial–distal; bl, buccal–lingual). The first digit of the location code (FDI-scheme) corresponds to the quadrant in the dentition, while the second digit indicates
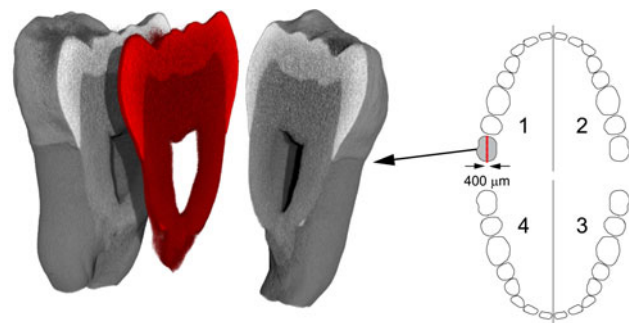

Fig. 1 Tooth slice 100818 was cut in occlusal–apical direction. The image shows a three-dimensional rendering of the specimen from a μCT scan of the entire tooth

Table 1 List of eight tooth slices included in this study

Specimen	Location	Cut direction	Code
100818	18	md	A
110448	48	md	B
110818	18	md	C
111038	38	md	D
111527	27	md	E
090148	48	bl	F
090748	48	bl	G
090937	37	bl	H

The location is according to the FDI-scheme. The cut direction md corresponds to mesial–distal (sagittal plane) and bl buccal–lingual (frontal plane)

the tooth, one being the first incisor and eight the third molar (cf. Fig. 1).

2.3 SRμCT Measurements

Synchrotron radiation-based micro computed tomography of the tooth slices (SRμCT) was performed at the beamline W2 at HASYLAB (DESY, Hamburg, Germany) operated by the Helmholtz Zentrum Geesthacht in standard absorption contrast mode [41]. Measurements were performed at photon energies of 45 and 48 keV. 1,441 projections with equidistant angular steps over 360° with asymmetric rotation axis were acquired. Because of the parallel beam, one can combine the two related projections [42] to reconstruct the data with a standard filtered back-projection algorithm as the data recorded with the symmetric rotation axis. Pixel sizes of 3.3 and 4.6 μm, respectively, were chosen. The radiographs were binned by a factor of two before reconstruction to improve the photon statistics and thereby the contrast [43]. The spatial resolution of the entire experimental setup was determined by the 10% value of the modulation transfer function of a radiograph from a highly X-ray absorbing edge [44]. It corresponded to 4.2 and 6.2 μm, respectively.

2.4 Scanning SAXS

Scanning small-angle X-ray scattering measurements (SAXS) were performed at the cSAXS beamline at the Swiss Light Source (PSI, Villigen, Switzerland). The specimens, placed in polyimide sachets to avoid dehydration during measurements, were mounted on a metallic frame and raster-scanned in 50 μm steps in horizontal and vertical directions through a 18.58 keV X-ray beam focused to 5×25 μm^2 spot size at the specimen location. Specimen to detector distance, determined from the first scattering order of a silver behenate specimen, amounted to 7.1 m. Three tooth slices, two carious and one healthy, were measured with two modules of the PILATUS 2 M detector while the remaining specimens were measured with 24 modules (full frame) [45]. To reduce air scattering, an evacuated flight tube was placed between specimen and detector. The X-ray attenuation of the specimens was measured before each scan with attenuated beam or inline with the SAXS scans. The air scattering signal was subtracted from each pattern.

2.5 SAXS Data Treatment

The numerous SAXS datasets were processed using self-written MATLAB® (2011a, The MathWorks, Natick, USA) routines. Each scattering pattern is divided into 16 azimuthal segments, and the intensity in each segment is integrated for further treatment. The resulting data comprise, for each scattering pattern, intensities for 16 azimuthal segments as a function of the radius that corresponds to the momentum transfer q. The average intensity in a q-range is plotted as a function of angular position and approximated by a cosine function through fast Fourier transform (FFT) [38]:

$$I(q) = I_0 + I_2 \cdot \cos(\phi + \Phi)$$

where I_0 and I_2 are the norm of the zero and second Fourier components respectively, and Φ is the phase of the second Fourier component. I_0 corresponds to the total mean scattered intensity and Φ yields the main orientation of the scattered intensity (cp. Fig. 2).

The central image in Fig. 2 shows the mean scattered intensity in the q-range corresponding to 20–30 nm from specimen 100818. Four SAXS patterns at selected locations from radial enamel, dentin-near enamel, enamel-near dentin and pulp-near dentin are displayed. The mean intensity between the two white circles is plotted for each pattern as function of the angular position. The dotted lines indicate the FFT-based cosine approximations.

Scattering signal orientation is determined from the phase of the related cosine, scattering anisotropy is related to the cosine amplitude and degree of orientation is defined as the ratio between the amplitude of the cosine and the total mean intensity. The latter is proportional to the abundance of nanostructures and their scattering cross sections. The orientation of the scattering is typically perpendicular to the scattering features like tubuli or fibers with the notable exception of the periodic structures. For example the 67 nm periodicity along collagen fibers creates a scattering signal along the fiber direction.

The sum of the absolute differences between cosine and data yields information on the specimen anisotropy as well appropriateness of the cosine approximation [38]. The total scattered intensity relates to the abundance of nanometer-sized scatterers in the indicated range, the degree of orientation to their anisotropy. The slope of the scattered
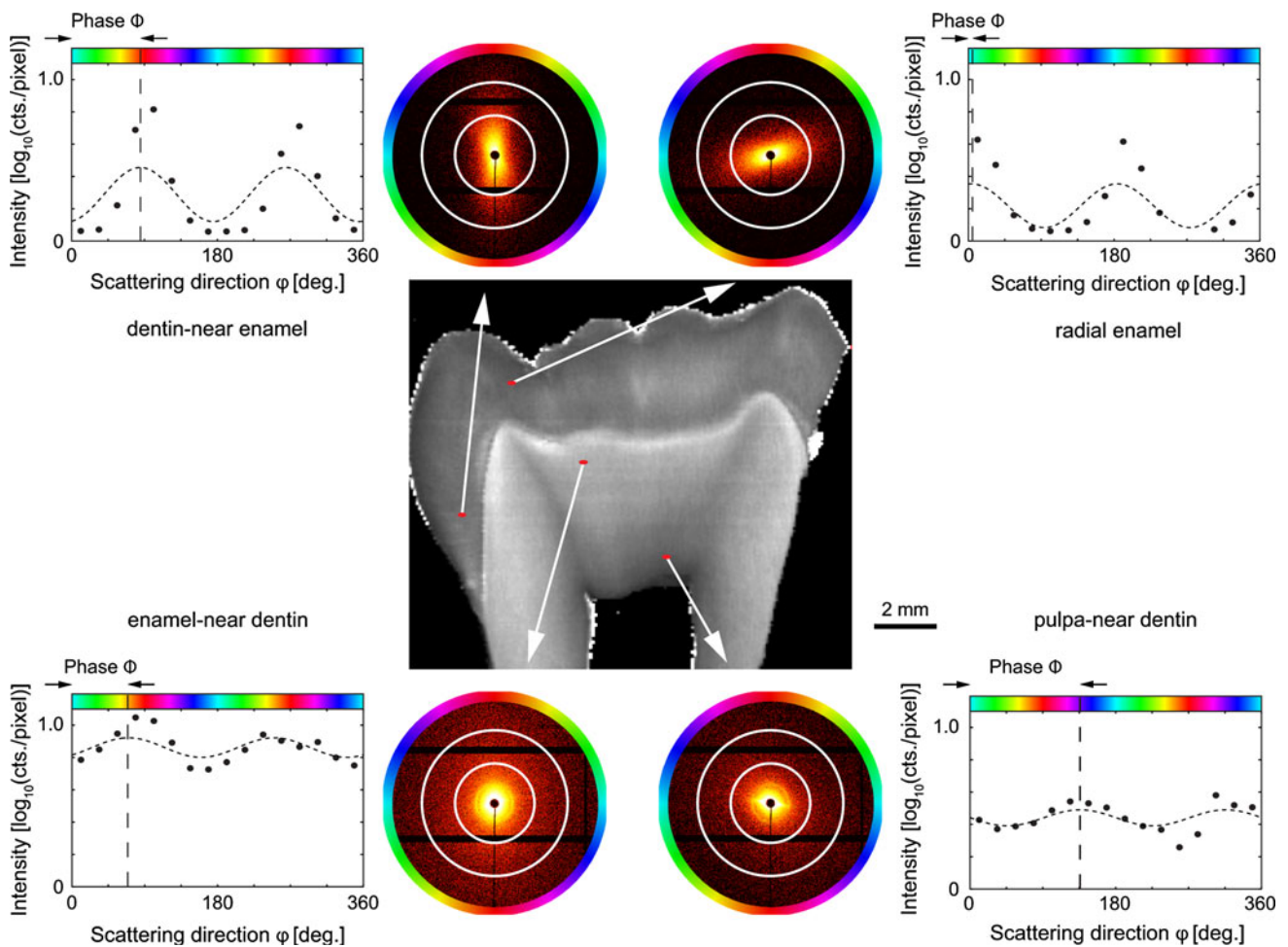
Fig. 2 The central image shows the mean scattering signal in the range corresponding to 20–30 nm of a 400 μm-thin tooth slice (specimen 100818). Scattering patterns were acquired in a 50 μm × 50 μm raster pattern. Four selected scattering patterns from radial enamel, dentin-near enamel, enamel-near dentin and pulp-near dentin are shown. Prominent differences in signal orientation and shape are apparent. Intensity in a selected q-range is plotted as function of the angular position and approximated by a cosine

intensity, plotted against the momentum transfer q, can be approximated as

$$I(q) \sim q^{-\alpha}$$

An intensity decay proportional with $\alpha = -1$ is characteristic for elongated, needle-like structures, $\alpha = -2$ indicates flat, disk-like structures while $\alpha = -4$ relates to volumetric structures [46].

Collagen features a characteristic periodicity of 67 nm along the fibril direction [8, 47, 48], resulting in a peak in the scattering pattern. This peak can be extracted by approximating the base intensity below the peak with a power-law with an exponent of -2.6 [40]. The scattered intensity above the curve is solely associated with the collagen. Considering only the collagen-related intensity allows determining the relative abundance of well-ordered collagen and the orientation of collagen on average over the area that has been illuminated, on the order of 100 μm² , for each point of an image. Figure 3 provides a

selection of signal channels for the characteristic specimen 100818. It shows the extracted collagen signal and the scattering signal in the q-range corresponding to 140–200 nm. The degree of orientation is defined as I_2/I_0 and is related on how strongly anisotropic the scatterers in the specimen are oriented. The deviation from cosine is the total absolute deviation of the data from the approximated cosine.

3 Results

3.1 Microanatomy of the Tooth Revealed by Scanning SAXS

Figure 4 shows, for specimens 100818 and 111038, the average scattered intensity, the orientation and the degree of orientation of a tooth slice, in the q-range corresponding to 50–100 nm as well as a slice through the SRμCT data.
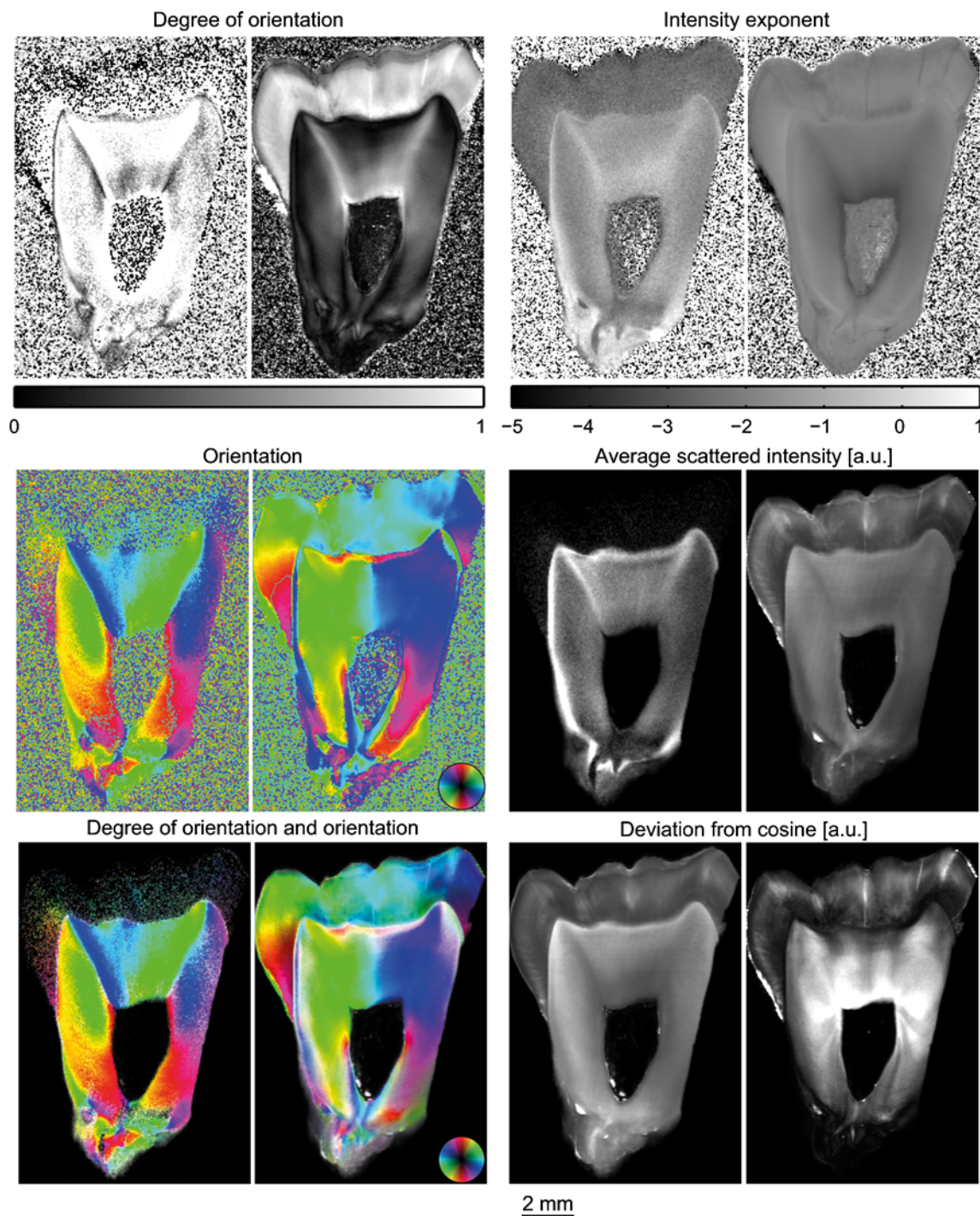
Fig. 3 Processed scanning SAXS data of specimen 100818 in the *q*-range corresponding to 140–200 nm on the *left* of each image pair, and the collagen-related signal on the *right*. The degree of orientation is defined as the ratio between anisotropic and isotropic scattered intensity, the mean orientation of the scattering signal is according to the *color-wheel*, the total mean scattered intensity relates to the abundance of nanometer-size scatterers, the deviation of the azimuthally integrated intensity from a cosine contains information similar to the degree of orientation, and the intensity exponent relates to the shape of the scatterers

The images of Fig. 5 support the non-specialist to discover the prominent microstructures well known from optical microscopy of tooth slices within the spatially resolved SAXS representations.

Specimen 111038 depicted in the lower half of Fig. 4 clearly exhibits a carious lesion in its center. In the images, the hard tissues, enamel and dentin, can be clearly distinguished. Hunter–Schreger bands [49], which arise due to

Fig. 4 Processed SAXS signal of specimens 100818 (no apparent caries) represented by the upper four images and 111038 represented by the lower four images (prominent caries) in the q-range corresponding to 50–100 nm and cuts through SRμCT data. Well-known features are made visible in the different channels. Ebners lines, Hunter–Schreger bands and striae of Retzius can best be identified in the total mean scattering signal (**a**), while overall tubule orientation can be spotted in the SRμCT data (**b**, **f**). The de-mineralized carious region yields a stronger scattering signal than the unaffected surrounding tooth hard tissue (**e**). The carious region is not apparent in the orientation channel (**h**)
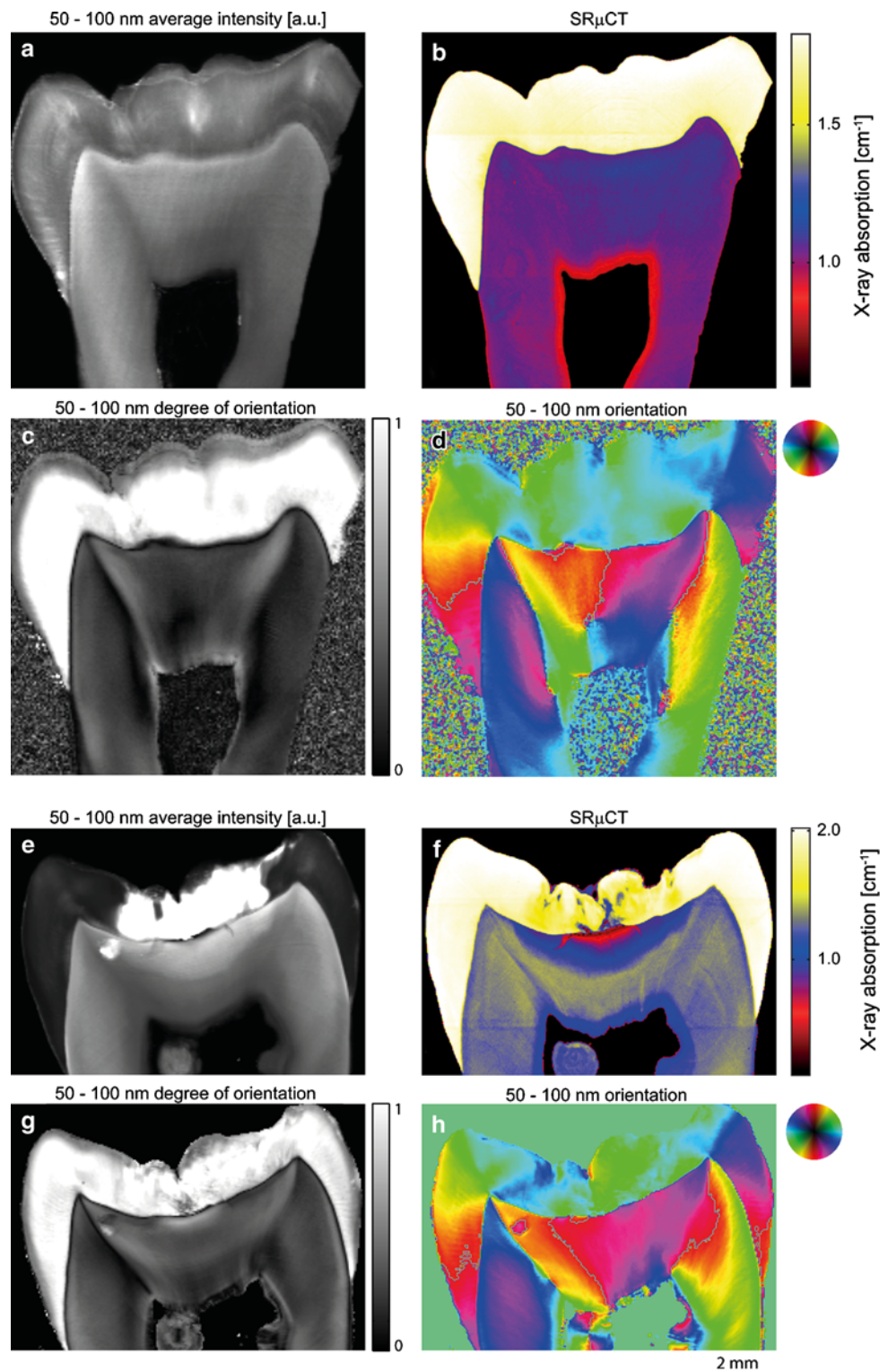
the decussation of neighboring bundles of enamel crystallites and run from the DEJ to the surface of the tooth, are identified as horizontal stripes in specimen 100818 image (a) on the left side in enamel. These bands are also visible as alternating stripes of higher and lower orientation in image (g) on the right side in enamel. Striae of Retzius [50] are visible in image (a) in the upper right part of the tooth slice as horizontal parallel lines to the enamel dentin boarder. These lines result from the deposition of layers of different calcification during tooth formation. In dentin, Ebner lines [51], also known as growth lines, which indicate the daily rate of dentin formation, and dentin tubules,
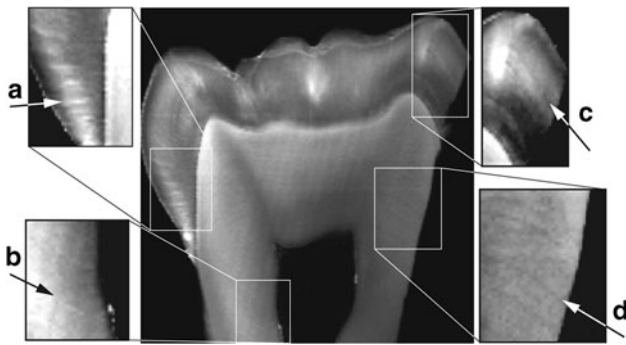
Fig. 5 Processed scanning SAXS data of specimen 100818. The enlarged picture details show regions where well known micro-anatomical features can be identified. In *a* Hunter–Schreger bands which result from the decussation of neighbouring rod bundles can be seen as alternating *bright and dark stripes*. In *b* the overall direction of the dentinal tubules, micrometer-thin channels in the dentin, can be identified. In *c* lines arising from the deposition of different calcification layers during enamel formation called lines of Retzius are shown, while in *d* the imbrication lines of von Ebner that correspond to the daily rate of dentin formation can be seen. The contrast and brightness of the detailed images has been modified with respect to the original image to better bring to light the microstructures

micrometer-thin canals which contain the long cytoplasmatic processes of odontoblasts and extend circularly from the pulp to the dentino-enamel and dentino-cemental junctions, are identified.

In the SRμCT image of Fig. 4b, cracks in enamel and an increase in X-ray absorption towards the tooth surface are observed. SRμCT of dentin shows a lower X-ray absorbing layer around the pulp. The direction of dentin tubules is clearly visible.

The bright spot seen in the upper left dentin corner of the processed SAXS data of specimen 111038 is not present in the SRμCT data and thus assumed to result from debris on the tooth slice and regarded as artifact.

3.2 Caries Affected Tooth

Caries-damaged tooth hard tissue of specimen 111038 represented in Fig. 4 exhibits increased scattering potential compared to unaffected regions, indicating increased porosity or larger crystallites [31, 52, 53].

Based on the degree of orientation, cf. Fig. 4g, the caries-affected part of the tooth slice cannot be segmented from the unaffected regions. There is only a spot visible, which is located in the dentin adjacent to the DEJ. The anisotropy of the nanostructures is only influenced by caries in regions of acute demineralization, i.e. in the final stages of disease. The carious region cannot be perceived in the images of the mean orientation of the scattering signal, as shown in Fig. 4h.

3.3 Enamel

The orientation of enamel crystallites, which are aligned along the enamel rods running from the DEJ towards the tooth surface, is reflected by the mean orientation of the scattering signal, being more or less parallel to the DEJ throughout the enamel, cf. Fig. 4d, h.

The scattering signal intensity of enamel is found to be inhomogeneous. Besides Hunter–Schreger bands, reflecting the decussation of crystallites, a gradual change of intensity between dentin-near and outer enamel is found at different q-ranges. Figure 6 shows the normalized average scattered intensity I_n for eight q-ranges. Total scattered intensity should not be directly compared between different q-ranges, as the intensity considerably decreases with the scattering angle. In order to compare the X-ray scattering of the different q-ranges, the mean intensity in enamel was integrated for each range and divided by the number of raster points in the enamel, yielding a normalization factor N_q. The normalized intensity I_n corresponds to the total average intensity at each point divided by N_q.

At larger scattering angles, corresponding to 10–20 and 20–30 nm, the average scattered intensity is larger towards the dentin, with its maximum in the center of the slice at the DEJ, and decreases towards the occlusal surface. With decreasing scattering angle, the intensity maximum shifts towards the occlusal surface, while regions of decreased intensity appear around the cusps.

In Fig. 7, the degree of orientation of the scattering signal is shown, which relates to the local anisotropy of the tooth slice. A band of less oriented structure is found at the enamel periphery towards the occlusal tooth surface for the entire nanometer range.

3.4 Mantle Dentin

The outermost layer of dentin adjacent to the enamel is often referred to as *mantle dentin*. It has been found to be of different composition compared to bulk dentin and to possess different mechanical properties [11–13, 16, 18, 47, 54, 55].

A thin layer exhibiting high scattering potential is found in dentin right adjacent to the DEJ (see Fig. 7, images in the first row) for both collagen and total scattering signal. The DEJ appears as thin black line in Fig. 4c, g indicating isotropic scattering signal, in contrast to enamel, where a high degree of orientation is present.

3.5 Bulk Dentin

Prominent intra-tooth changes in SAXS signal along the dentin are apparent. Figure 7 shows data from specimen 100818. Reduced mean intensity is found around the pulp
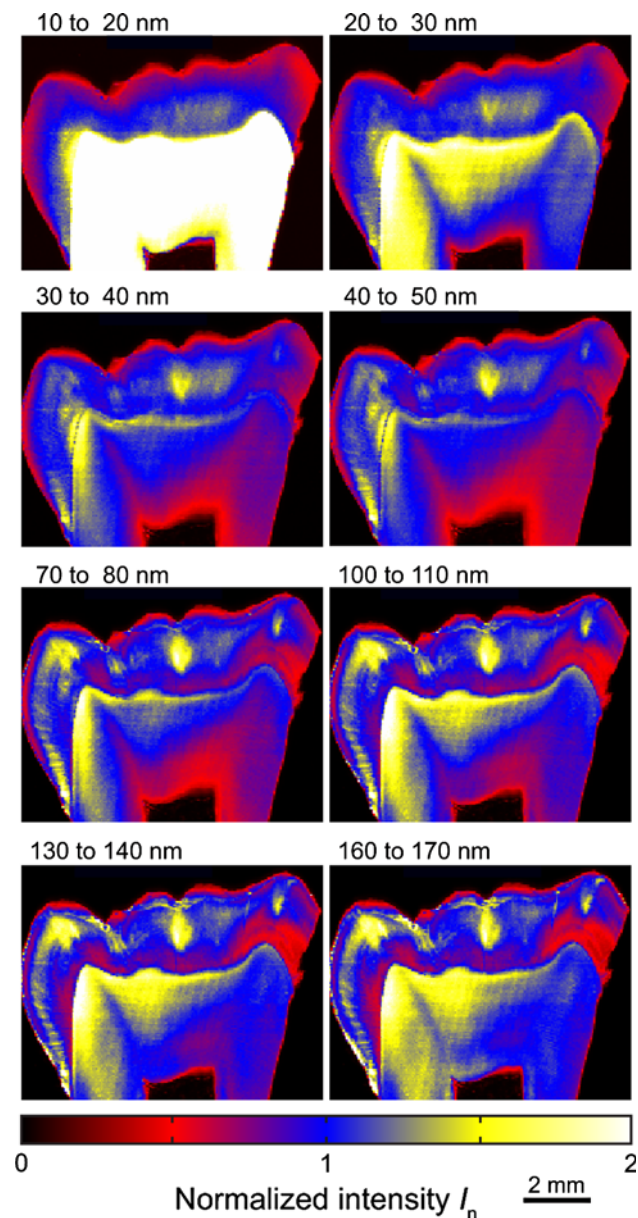
Fig. 6 Total normalized scattered intensity I_n of specimen 100818 at eight q-ranges. In the enamel, at larger scattering angles corresponding to 10–20 nm, the total mean scattered intensity is larger towards the dentin, with its maximum in the center of the slice at the DEJ, and decreases towards the occlusal surface. With decreasing scattering angle, the intensity maximum shifts towards the occlusal surface. The average scattered intensity of the enamel has been averaged to unity for each range

and increases towards the outer regions of dentin. At q-ranges corresponding to structures above 100 nm, a bright halo appears surrounding the pulp cavity.

Changes are gradual except along virtual lines connecting the tooth cusps with the pulp. In the average scattering signal these lines are less pronounced and present themselves as regions of decreased intensity. They are clearer in the collagen-related signal, where they appear as

bright bands. The ratio between organic and inorganic components might be shifted in favor of the organic structures along these lines. This internal interface becomes better visible and is sharper in the degree of orientation channel. An acute drop and subsequent increase in nanostructure anisotropy is observed at larger scattering angles and in the extracted collagen signal, when going from the outer regions of dentin towards the slice center. The reduced anisotropy is, however, not observed towards larger structures. For the entire nanometer range, increased anisotropy is observed in a thin layer around the pulp.

Orientation in dentin appears to be more or less perpendicular to structures in enamel, presenting angles close to 0° to the DEJ, indicating perpendicular orientation of collagen to dentinal tubules, in reasonable agreement with results from literature [47].

The collagen-related signal runs perpendicularly to that of dentin, indicating a parallel alignment of fibers and crystallites. Again, changes in orientation in dentin are gradual except along internal interfaces, which, in the ranges up to 100 nm and for the collagen signal, coincide with the ones found for the degree of orientation channel.

4 Discussion

The studies of tooth structure and organization have generally followed technological advances in imaging techniques. Long ago, light microscopy was used to identify large long-range micro-structural features such as tubules and von Ebners lines in dentin, and striae of Retzius and Hunter–Schreger bands in enamel. Scanning and transmission electron microscopy allowed for the identification of local details of rods and crystallites in enamel, and of tubules and their collagenous matrices in dentin. However, little attention has been directed to understand the tooth-wide organization of nanometer-sized structural components, hydroxyapatite crystallites and collagen. Scanning SAXS allows quantifying tooth nanostructures over macroscopic areas, allowing identifying short- and long-range ordering in the plane perpendicular to the incident X-ray beam. In Fig. 8 nanostructure-related scattering signal orientation (left) and, for collagen-specific scattering, a signal, which is the combination of mean intensity, orientation and degree of anisotropy (right) of eight tooth slices from different patients are shown. Slices (a) through (e) were cut in mesial–distal, while slices (f) through (h) in buccal–lingual directions. Although differences can be spotted between the specimens, the overall similarity of their individual architecture is striking, demonstrating unified tooth-wide organization at the level of collagen fibers and hydroxyapatite crystallites.
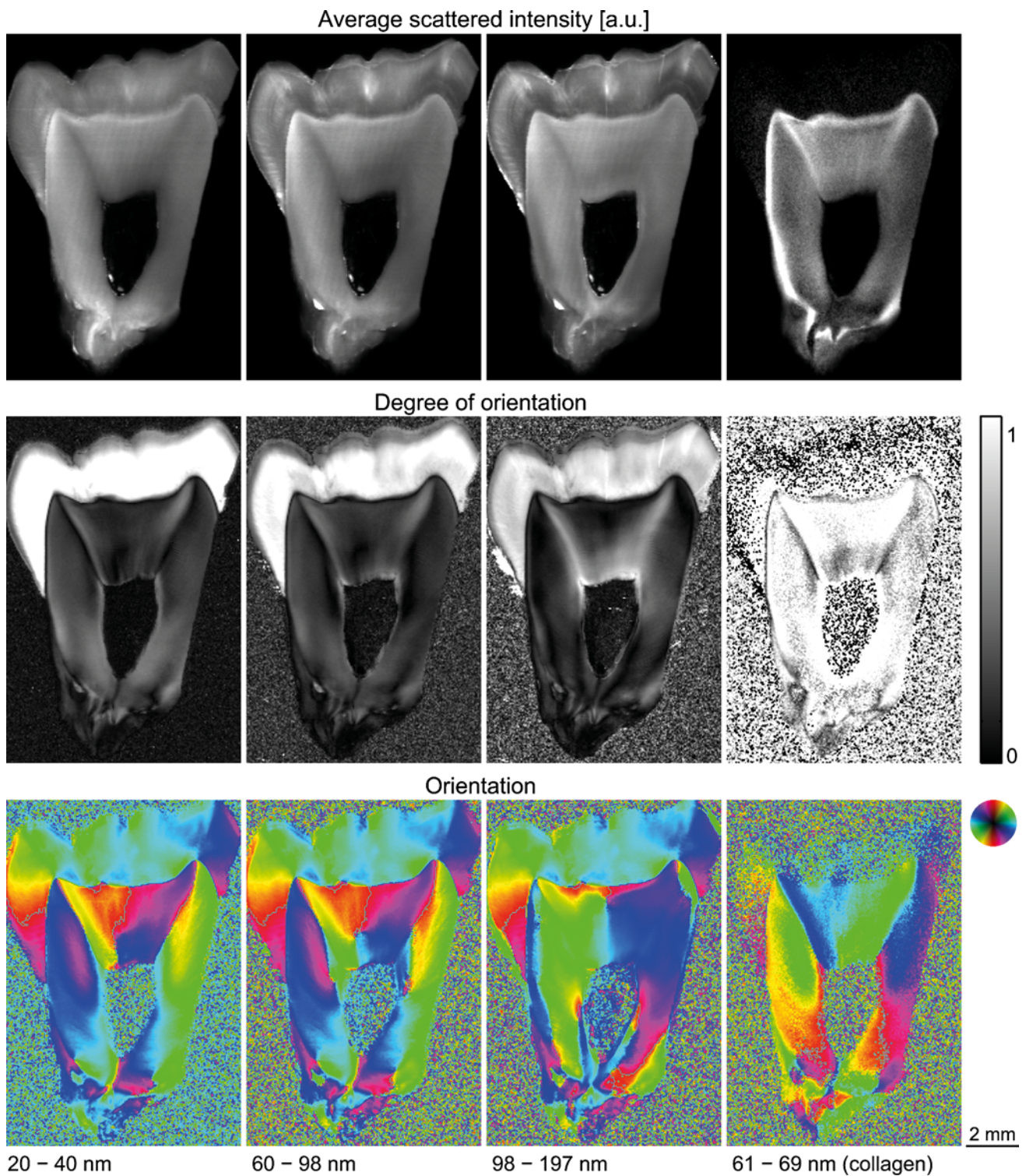
Fig. 7 The figure shows the processed SAXS signal of specimen 100818 for three q-ranges and for the collagen related signal. A distinctive feature in the dentin on a virtual line connecting the cusps with the pulp can be identified. While the collagen yields stronger scattering along these lines, reduced intensity is found at all other ranges. Sharp changes in scattering signal orientation and degree of orientation can also be seen

Morphological changes of the nanometer-size components are made visible with micrometer resolution, allowing uncovering the hierarchical organization of tooth structures. Because of the X-ray beam area of 25 μm × 5 μm used for the scanning SAXS measurements presented here, it is possible to identify structural changes on the
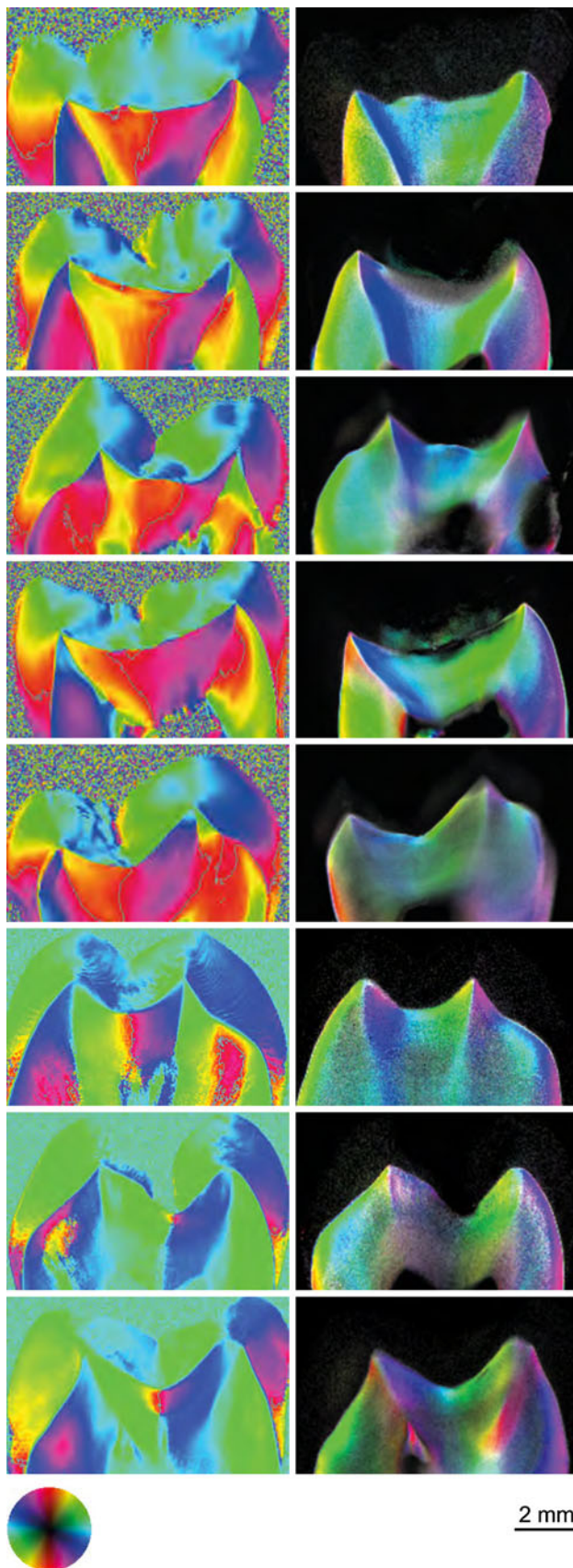
◀**Fig. 8** Processed scanning SAXS signal from specimens obtained from eight teeth, listed in Table 1. Strong similarity of the overall organization of tooth nano-anatomy is found. The *left column* shows the orientation of nanostructures in the range from 8 to 20 nm. The *right column* combines orientation (*color-wheel*), scattering intensity (*color brightness*) and anisotropy (*color saturation*) of the collagen-related signal. The orientation of the scattering signal (*left column*) is perpendicular to the nanostructure orientation, while the orientation of the collagen-related signal (*right column*) is parallel to the fibers

entire nanometer scale that are visible after averaging nanoscale features over the X-ray spot size. The information obtained is the exact average over the nanometer-size scatterers within the illuminated volume projected in beam direction. In order to obtain the complete three-dimensional (3D) information of the nanostructures, one has to investigate the specimen under different rotation angles.

Hunter–Schreger bands are an optical effect caused by synchronous decussation of bundles of enamel rods [56]. Lynch et al. [57] reported that the width of these bands ranges from 70 to 400 μm, depending on their location in the tooth, with the largest ones being located in the cervical region. The decussation implies a change in orientation of the nanometer-sized enamel crystallites [24]. Thus, Hunter–Schreger bands are prominently visible in the cervical regions in the SAXS data, as can be seen in the images of Figs. 4a, c, d, 8f, g. Similarly, striae of Retzius and Ebner lines can be identified when the spacing between them are sufficiently large.

4.1 Data Treatment

SAXS datasets of tooth slices consist of 30,000 or more individual scattering patterns. To process this huge amount of data, automation is needed. In azimuthal segments radially integrated SAXS data are approximated by a cosine through an FFT algorithm, see above. When the scattering specimen does exhibit a moderate degree of orientation, as is the case for dentin, deviation from a perfect cosine is small (cf. Fig. 2). The inversion symmetry of scattering patterns can be exploited to compensate drawbacks of the modular detector structure of the PILATUS 2M, where no photons can be detected in the gaps between the detector modules.

When the scattering from the specimen is strongly anisotropic, however, the deviation from a cosine increases, as can be seen from the enamel pattern in Fig. 2, especially when highly oriented scattering occurs, i.e. sharp peaks over a rather flat background appear in the azimuthal plot. In these cases the scattering anisotropy or degree of orientation can be underestimated. Nonetheless, the calculated degree of orientation correlates with scattering signal anisotropy. Strongly oriented scatterers yield a high

degree of orientation, even though the magnitude of the signal might be underestimated. The mean orientation of the scattering signal, related to the phase of the cosine, is extracted correctly, as it is the case for the mean intensity.

4.2 Enamel

SAXS data reveals a narrow band of reduced orientation at the enamel surface on the length-scale range from 8 to 200 nm. Its width is specimen-dependent and ranges from 150 to 500 μm. Both the first-formed enamel near the DEJ, and the last-formed enamel on the outer surface differ from bulk enamel; these thin layers of specialized enamel are often termed *aprismatic enamel*. The thicknesses of the last-formed enamel band identified in SAXS data, however, are much wider than the commonly reported 100 μm. Due to the uneven tooth surface anatomy, the edges of the tooth slices of finite thickness present skewed edges, especially on the occlusal surface. Due to the projective nature of scanning SAXS, a larger area of surface-near enamel is imaged. We believe that the broadened band of reduced orientation near the tooth corresponds to the specialized last-formed enamel, and the recorded width is affected by the edge effect.

A comparable situation exists with the first-formed enamel adjacent to the DEJ. In Fig. 4c a dark band can be seen along the interface between enamel and dentin. It is rather sharp at the flanks of the tooth and appears broadened towards the center. Again, the tilted boundary between enamel and dentin can explain the broadening. This is supported by the appearance of the DEJ in Fig. 4a. It appears blurred towards the center of the slice, while it is sharp near the flanks indicating tilted resp. parallel alignment of the DEJ with the X-ray beam. However, microhardness, strain, and X-ray data have suggested that the zone specialized first-formed enamel may be much thicker than derived from microscopy [15, 58, 59].

The mean scattered intensity in enamel is increased near the DEJ in comparison with the surrounding in q-ranges corresponding to structures smaller than 30 nm (cp. Fig. 6). At q-ranges corresponding to larger structures the region of maximal intensity shifts outwards. A region of reduced intensity appears around the cusps near the DEJ.

The enamel crystallite size has been the matter of a multitude of investigations ([60] and references therein). The results vary in a broad range concerning diameters, ranging from 10 to 50 nm and length up to 600 nm, although lengths of 1 μm have been reported ([61] and references therein). Our findings can be explained by assuming a well-defined distribution of crystallite sizes within the enamel, with smaller crystallites near the DEJ and larger ones towards the outer enamel. However, it is generally believed that all bulk enamel, except first-formed

and last-formed enamel is equal concerning crystallite size. The inhomogeneous 3D-orientation might play a role. Crystallites oriented parallel to the incident X-ray beam present a smaller cross-section, thus yielding a broader SAXS pattern. As the orientation of the scatterers in SAXS is only accessible in the plane perpendicular to the X-ray beam, an additional measurement of a tooth slice through the enamel in horizontal cut should be performed. Alternatively, the observation can be related to zones of high protein concentration, which correspond to the regions [62], which yield increased scattering at small ranges below 30 nm.

4.3 Mantle Dentin

It is well known that in bulk dentin collagen is arranged perpendicular to dentin tubules [47]. The dentin region adjacent to the DEJ, sometimes termed *mantle dentin*, contains only few tubules and practically no peri-tubular dentin [12], and lower mineral content [11]. Because mantle dentin exhibits lower mineralization and higher collagen content [18] than bulk dentin, the DEJ is tougher than bulk dentin or enamel [16]. Imbeni et al. [13] concluded that the collagen orientation at the DEJ is a key factor in the reinforcing mechanism. Near the DEJ, orientation of the collagen fibers changes to be parallel to tubules [16, 54, 55]. It has been suggested that collagen fibers cross the DEJ from dentin into enamel [16, 63], contributing considerably to the bonding of the two tooth hard tissues. The increased intensity of the collagen-related signal visible in Fig. 7 is in perfect agreement with the expected higher concentration of collagen in this region. We speculate that the decreased degree of orientation observed (cf. Fig. 7, central row, collagen signal), is related to the change in orientation of the fibrils. The SAXS signal yields the average over the illuminated area defined by the finite X-ray spot size of 5×25 μm^2. Thus, in this transition zone from parallel to perpendicular orientations of the fibrils, the anisotropy of the SAXS patterns is diminished by averaging over both orientations.

Similar to the collagen-related signal, higher intensity is found in mantle dentin at the entire nanometer scale. The obvious conclusion that this is the result of an increased number of scatterers, i.e. crystallites, contrasts with the low mineralization of mantle dentin. However, the scattered intensity is not directly proportional to the degree of mineralization, as can for example be observed in carious lesions (cf. Fig. 4). Massive demineralization is present, as can be seen in the SRμCT image. Nonetheless, the carious regions exhibit massively increased scattering intensity. A potential explanation could be an increased contrast and thereby scattering cross section caused by increased density variations like porosity.

4.4 Dentin

Orientation of dentin crystallites and collagen as determined by our SAXS measurements are in reasonable agreement with literature [7, 10, 11, 31, 32, 39, 47, 63, 64]. We additionally extracted the degree of orientation as a measure of local specimen anisotropy. A similar examination on collagen in dentin was performed by Kinney et al. [47]. In that study, horizontal tooth slices were examined by SAXS. They concluded that collagen orientation was less pronounced in pulp-near dentin and increased towards the tooth flanks, in apparent contradiction with the results shown here, where high collagen orientation is found in a 0.5–1 mm-thick region around the pulp flanks. We believe the cutting direction of the tooth slice is crucial. As can be seen in Fig. 7, collagen appears to be oriented parallel to the pulp walls in this region, indicating a vertical alignment of collagen fibers. Observation of horizontal tooth slices would result in a cross-sectional view of parallel fibers, therefore resulting in no preferred orientation.

The same pulp-near region exhibits lower X-ray absorption compared to the rest of dentin. Although limited information is available about the organization of secondary dentin, we assume that this layer is the result of dentin apposition after tooth completion. This implies that the highly oriented collagen adjacent to the pulp is secreted after tooth completion.

The abrupt changes in tooth nanostructure orientation observed in dentin and collagen at sizes up to 100 nm has also been reported by Märten et al. [31]. We assume this interface results when the paths of odontoblasts converge their way from the DEJ to the center of the tooth during dentin formation. The position of this internal interface within the tooth along virtual lines connecting the pulp with the tooth cusps suggests a relationship with the mechanical properties of the tooth.

4.5 Carious Lesions

Tooth hard tissue in regions affected by caries exhibits strongly increased scattering potential [31, 40]. Takuma et al. [53] reported an increase in crystallite size in carious dentin, confirmed by Märten et al. [31]. An increase in crystallite size could explain stronger scattering, at least at smaller scattering angles. Strong intensity, however, is observed at all investigated q-ranges. Therefore, an increase in crystallite size as sole explanation seems implausible. Caries is known to increase porosity in enamel [52]. If similarly, increased porosity is induced in dentin, this explains stronger scattering potential. However, SAXS is not the method of choice for the quantification of porosity, as it does not allow discriminating which contribution to the scattering pattern originates from pores and which from material. Therefore, further investigations with complementary imaging techniques are needed to fully understand this phenomenon.

4.6 Bio-Inspired Treatments of Teeth: Nanodentistry

Currently dentists restore teeth with materials that do not resemble to the micro- and nanostructures of natural teeth including their well-aligned, anisotropic inorganic and organic components. The lifetime of these isotropic restorations is quite long but generally limited.

Recent results including scanning SAXS provide a detailed insight into the complex morphology and structure of the inhomogeneous tooth hard tissues [20, 31, 32, 39, 40]. Given the complex architecture of the tooth, building artificial tooth restorations from different components for dentin and enamel with strong anisotropies could be beneficial. How far the variations within enamel and dentin, respectively, have to be considered is still an open question.

Another route of caries treatment is related to stop the disease and trying to re-mineralize the dentin and enamel with the aim to re-establish the natural tooth or at least significant parts of it [65–67]. Here, nanotechnology might be of upmost importance as nanometer-size calcium phosphates tend to nucleate at the nanometer-size collagen fibrils [68, 69]. Their nucleation at the collagen fibers has to be understood in certain detail to become successful.

5 Conclusion

We demonstrated that scanning SAXS yields the well-known features like Hunter–Schreger bands etc. Through the possibility of imaging the tooth-wide organization of nanostructures we identified an internal interface within dentin, where a sharp change of orientation of the nanostructures occurs. Furthermore, strong anisotropy in enamel with inverse trends of scattering intensity for different q-ranges has been revealed. For future developments of nature-analogue dental materials it seems mandatory to consider the nanostructure of teeth to achieve improved long-term results for dental restorations. High-resolution scanning SAXS experiments and their detailed analysis will provide a sound basis for nanotechnology-based dental treatments we may term *nanodentistry*.

References

1. Steele JG, Sanders AE, Slade GD, Allen PF, Lahti S, Nuttall N, Spencer AJ (2004) Commun Dent Oral Epidemiol 32(2):107–114
2. Akifusa S, Soh I, Ansai T, Hamasaki T, Takata Y, Yohida A, Fukuhara M, Sonoki K, Takehara T (2005) Gerodontology 22(2):91–97
3. Miyaura K, Matsuka Y, Morita M, Yamashita A, Watanabe T (1999) J Oral Rehabil 26(3):223–227
4. Meinl A, Tangl S, Pernicka E, Fenes C, Watzek G (2007) J Forensic Sci 52(2):438–441
5. Kinney JH, Marshall SJ, Marshall GW (2003) Crit Rev Oral Biol Med 14(1):13–29
6. Yan J, Taskonak B, Mecholsky JJ Jr (2009) J Mech Behav Biomed Mater 2(5):478–484
7. Elbaum R, Tal E, Perets AI, Oron D, Ziskind D, Silberberg Y, Wagner HD (2007) J Dent 35(2):150–155
8. Habelitz S, Balooch M, Marshall SJ, Balooch G, Marshall GW (2002) J Struct Biol 138:227–236
9. Leventouri T, Antonakos A, Kyriacou A, Venturelli R, Liarokapis E, Perdikatsis V (2009) Int J Biomater 2009:698547
10. Porter AE, Nalla RK, Minor A, Jinschek JR, Kisielowski C, Radmilovic V, Kinney JH, Tomsia AP, Ritchie RO (2005) Biomaterials 26(36):7650–7660
11. Tesch W, Eidelman P, Roschger P, Goldenberg F, Klaushofer K, Fratzl P (2001) Calcif Tissue Int 69:147–157
12. Coutinho ET, Moraes JR, Paciornik S (2007) Mater Res 10(2):153–159
13. Imbeni V, Kruzic JJ, Marshall GW, Marshall SJ, Ritchie RO (2005) Nat Mater 4:229–232
14. Shimizu D, Macho GA (2007) J Hum Evol 52(1):103
15. White SN, Paine ML, Luo W, Sarikaya M, Fong H, Yu Z, Li ZC, Snead ML (2000) J Am Ceram Soc 83(1):238
16. Lin CP, Douglas WH, Erlandsen SL (1993) J Histochem Cytochem 41(3):381–388
17. Pioch T, Golfels D, Staehle HJ (1992) Dental Traumatol 8(6):241–244
18. Lin CP, Douglas WH (1994) J Dent Res 73(5):1072
19. White SN, Miklus VG, Chang PP, Caputo AA, Fong H, Sarikaya M, Luo W, Paine ML, Snead ML (2005) J Prosthet Dent 94(4):330
20. Zaslansky P, Zabler S, Fratzl P (2010) Dental Mater 26:e1–e10
21. Gallagher RR, Demos SG, Balooch M, Marshall GW, Marshall SJ (2003) J Biomed Mater Res Part A 64(2):372–377
22. Habelitz S, Marshall SJ, Marshall GW, Balooch M (2001) J Struct Biol 135:294–301
23. Xu C, Yao X, Walker MP, Wang Y (2009) Calcif Tissue Int 84(3):221–228
24. Boyde A (1989) Enamel. In: Oksche A, Vollrath L (eds) Teeth. Springer, Berlin, pp 309–473
25. Gruner JW, McConnell D, Armstrong WD (1937) J Biol Chem 121(2):771–781
26. Fejerskov O, Josephsen K, Nyvad B (1984) Caries Res 18(4):302–314
27. White SN, Luo W, Paine ML, Fong H, Sarikaya M, Snead ML (2001) J Dent Res 80(1):321–326
28. Boyde A (1987) Adv Dent Res 1(2):135
29. Macho GA, Jiang Y, Spears IR (2003) J Hum Evol 45(1):81–90
30. De Menezes-Oliveira MA, Torres CP, Gomes-Silva JM, Chinelatti MA, Menezes FCD, Palma-Dibb RG, Borsatto MC (2009) Microsc Res Tech 73(5):572–577
31. Märten A, Fratzl P, Paris O, Zaslansky P (2010) Biomaterials 31:5479–5490
32. Deyhle H, Bunk O, Buser S, Krastl G, Zitzmann NU, Ilgenstein B, Beckmann F, Pfeiffer F, Weiger R, Müller B (2009) Proc of SPIE 7401:74010E
33. Johansen E, Parks HF (1960) J Biophys Biochem Cytol 7(4):743–746
34. Lenz H (1961) Arch Oral Biol Spec Suppl 4:34–39
35. Ohgushi K, Fusayama T (1975) J Dent Res 54:1019–1026
36. Marshall GW, Balooch M, Gallagher RR, Gansky SA, Marshall SJ (2001) J Biomed Mater Res 54:87–95
37. Fratzl P, Jakob HF, Rinnerthaler S, Roschger P, Klaushofer K (1997) J Appl Crystallogr 30:765–769
38. Bunk O, Bech M, Jensen TH, Feidenhans'l R, Binderup T, Menzel A, Pfeiffer F (2009) New J Phys 11:123016
39. Müller B, Deyhle H, Bradley D, Farquharson M, Schulz G, Müller-Gerbl M, Bunk O (2010) Eur J Nanomed 3:30–33
40. Deyhle H, Bunk O, Müller B (2011) Nanomed Nanotechnol Biol Med. doi:10.1016/j.nano.2011.09.005
41. Beckmann F, Herzen J, Haibel A, Müller B, Schreyer A (2008) Proc of SPIE 7078:70781D
42. Müller B, Bernhardt R, Weitkamp T, Beckmann F, Bräuer R, Schurigt U, Schrott-Fischer A, Glueckert R, Ney M, Beleites T, Jolly C, Scharnweber D (2007) Int J Mater Res 98(7):613–621
43. Thurner P, Beckmann F, Müller B (2004) Nucl Instr Meth B 225(4):599–603
44. Müller B, Thurner P, Beckmann F, Weitkamp T, Rau C, Bernhardt R, Karamuk E, Eckert L, Buchloh S, Wintermantel E, Scharnweber D, Worch H (2002) Proc of SPIE 4503:178–188
45. Kraft P, Bergamaschi A, Broennimann C, Dinapoli R, Eikenberry EF, Henrich B, Johnson I, Mozzanica A, Schlepütz CM, Willmott PR, Schmitt B (2009) J Synchrotron Radiat 16:368–375
46. Guinier A, Fournet G (1955) Small angle scattering of X-rays. Wiley, New York
47. Kinney JH, Pople JA, Marshall GW, Marshall SJ (2001) Calcif Tissue Int 69:27–31
48. Balooch M, Habelitz S, Kinney JH, Marshall SJ, Marshall GW (2008) J Struct Biol 162:404–410
49. Mortell JF, Peyton FA (1956) J Dent Res 35(5):804–823
50. Wilson DF, Shroff FR (1970) Aust Dent J 15(3):162–171
51. Kawasaki K, Tanaka S, Ishikawa T (1979) Arch Oral Biol 24(12):939–943
52. Robinson C, Shore RC, Brookes SJ, Strafford S, Wood SR, Kirkham J (2000) Crit Rev Oral Biol Med 11:481–495
53. Takuma S, Tohda H, Watanabe K (1986) J Electron Microsc 35:60–65
54. Johnson NW, Poole DFG (1967) Nature 213(5077):695–696
55. Zaslansky P, Friesem AA, Weiner S (2006) J Struct Biol 153(2):188–199
56. Osborn JW (1990) Arch Oral Biol 35(11):869–878
57. Lynch CD, O'Sullivan VR, Dockery P, McGillycuddy CT, Sloan AJ (2010) J Anat 217:106–115
58. Elliot JC, Anderson P, Gao XJ, Wong FSL, Davis GR, Dowker SEP (1994) J X ray Sci Technol 4:102–117
59. Wang RZ, Weiner S (1998) J Biomech 31:135–141
60. Grove CA, Judd G, Ansell GS (1972) J Dent Res 51(1):22–29
61. Johansen E (1964) J Dent Res 43(6):1007–1020
62. Weatherell JA, Robinson C (1973) The inorganic composition of teeth. In: Zipkin I (ed) Biological mineralization. Wiley, New York, pp 43–74
63. Arsenault AL, Robinson BW (1989) Calcif Tissue Int 45:111–121

64. Schmidt WJ, Keil A (1958) Die gesunden und die erkrankten Zahngewebe des Menschen und der Wirbeltiere im Polarisationsmikroskop. Theorie, Methodik, Ergebnisse der optischen Strukturanalyse der Zahnhartsubstanzen samt ihrer Umgebung. Carl Hanser Verlag, Munich

65. Kernen F, Waltimo T, Deyhle H, Beckmann F, Stark W, Müller B (2008) Proc of SPIE 7078:70780M

66. Bertassoni LE, Habelitz S, Pugach M, Soares PC, Marshall SJ, Marshall GW (2010) Scanning 32:312–319

67. Forsback AP, Areva S, Salonen JI (2004) Acta Odontol Scand 62(1):14–20

68. Höling HJ, Arnold S, Plate U, Stratmann U, Wiesmann HP (1997) Adv Dent Res 11:462–466

69. Trautz OR, Bachara BN (1963) Arch Oral Biol 8:601–613